Measuring Point Defect Density in Individual Carbon Nanotubes Using Polarization-Dependent X-ray Microscopy

Alexandre Felten,[†,*] Xavier Gillon,[†] Michal Gulas,[†] Jean-Jacques Pireaux,[†] Xiaoxing Ke,[‡] Gustaaf Van Tendeloo,[‡] Carla Bittencourt,[§] Ebrahim Najafi,[⊥] and Adam. P. Hitchcock[⊥]

[†]PMR, Facultés Universitaires Notre-Dame de la Paix (FUNDP), Namur, Belgium B-5000, [‡]EMAT, University of Antwerp, Antwerp, Belgium B-2610, [§]LCIA, University of Mons, Mons, Belgium B-7000, and [⊥]Chemistry & Chemical Biology, McMaster University, Hamilton, Canada L8S4M1

ABSTRACT The presence of defects in carbon nanotubes strongly modifies their electrical, mechanical, and chemical properties. It was long thought undesirable, but recent experiments have shown that introduction of structural defects using ion or electron irradiation can lead to novel nanodevices. We demonstrate a method for detecting and quantifying point defect density in individual carbon nanotubes (CNTs) based on measuring the polarization dependence (linear dichroism) of the C 1s $\rightarrow \pi^*$ transition at specific locations along individual CNTs with a scanning transmission X-ray microscope (STXM). We show that STXM can be used to probe defect density in individual CNTs with high spatial resolution. The quantitative relationship between ion dose, nanotube diameter, and defect density was explored by purposely irradiating selected sections of nanotubes with kiloelectronvolt (keV) Ga^+ ions. Our results establish polarization-dependent X-ray microscopy as a new and very powerful characterization technique for carbon nanotubes and other anisotropic nanostructures.

KEYWORDS: NEXAFS · carbon nanotube · X-ray spectromicroscopy · irradiation

Theoretical and experimental evidence indicate that structural defects in carbon nanotubes (CNTs) dramatically alter their physical, mechanical, and electronic properties.[1] Defects are known to reduce mechanical strength and Young modulus of the CNT and disrupt their electrical and phonon conductivity.[2,3] However, controlled introduction of defects can improve device performance for specific applications. Site-selective functionalization of CNTs was performed by Raghuveer *et al.* using focused ion beam irradiation (FIB) with subsequent chemical treatment.[4] FIB-generated defects are more reactive toward chemical species than pristine parts of the nanotube. Gomez-Navarro *et al.*[5] have shown that the resistance of single-walled CNTs (SWCNTs) can be tuned by defects created using Ar^+ irradiation. Plasma treatment of carbon nanotubes, which induces active sites and defects, is used to tailor size and distribution of metallic nanoparticles evaporated on the nanotube surface.[6] Gas sensors based on defective nanotubes also show improved sensitivity.[7] Recently, high-energy electron and ion beams have been employed to intentionally damage CNTs, changing their morphologies, welding tubes together, and soldering them to metal plates.[8−10]

Particle irradiation damages materials mainly through ionization and knock-on processes.[11] In materials such as CNTs, ionization is often quenched while knock-on collisions transfer energy and momentum to the target atoms, causing atomic displacements or atom removal.[12] In multiwalled carbon nanotubes (MWCNTs), radiation defects result in rupture, tilting, and bending of the basal planes. Prolonged exposure shrinks MWCNTs and eventually removes their central hollow core.[13]

To control the quality of as-grown CNTs and to study intentionally irradiated nanotubes, it is necessary to develop tools that are able to localize, characterize, and quantify defects on individual nanotubes. Existing methods, such as micro-Raman, anchoring of metal nanoparticles at defect sites, high-resolution transmission electron microscopy, Rayleigh and Raman scattering, and photoemission spectroscopy, are either not quantitative or show limited spatial resolution. In this paper, we demonstrate a new method to visualize defect density spatial distributions in pristine and ion beam damaged MWCNTs based on STXM.[1,14−17]

STXM is a synchrotron-based technique that combines near-edge X-ray absorption fine structure (NEXAFS) spectroscopy and focused probe microscopy to image and measure material properties at high spatial

*Address correspondence to alexandre.felten@fundp.ac.be.

Received for review February 4, 2010 and accepted July 01, 2010.

Published online July 7, 2010.
10.1021/nn1002248

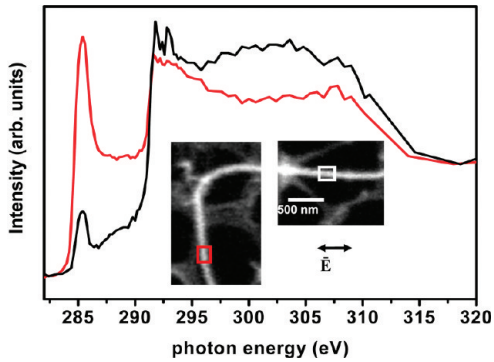

Figure 1. Linear dichroism of individual MWCNTs. Carbon 1s NEXAFS spectra of an individual MWCNT. The spectra were extracted from the red and white regions indicated in the inset STXM images, recorded at 292 eV. The red and black curves correspond to the spectra of the same nanotube oriented either parallel or 90° relative to the E-vector.

resolution. The state-of-the-art spatial resolution in STXM is better than 15 nm, although the spatial resolution employed in this work was 30 nm. In STXM, monochromatic X-rays are focused to a small area, and images are made by raster scanning the specimen through the focal point while simultaneously recording the intensity of the transmitted light.[18] The photon energy is varied to probe X-ray absorption spectral properties. STXM employs linearly polarized X-rays, and therefore, it can determine local anisotropy and structural order of materials at microscopic levels. Recently, we have shown that the C 1s $\rightarrow \pi^*$ transition from individual MWCNTs measured in STXM exhibits strong linear dichroism.[19,20] Electron energy loss in transmission electron microscopes (TEM-EELS) provides outstanding spatial resolution and, in principle, has an analogous sensitivity to anisotropic electronic structure through q-dependent EELS.[21−23] However, to date, q-dependent TEM-EELS has not been used to study the analogue of the dichroic signal we are exploiting in this work to characterize point defects in CNTs.

In this work, we have used controlled ion bombardment to selectively damage regions of MWCNTs and then measured the linear dichroism of these regions in STXM. Correlation of ion dose with modification of the π^* dichroism is used to explore the extent to which there is a quantitative relationship of the dichroic signal to local density of defects.

RESULTS AND DISCUSSION

Figure 1 plots the C 1s NEXAFS spectra of an individual MWCNT, with the CNTs oriented both vertically and horizontally relative to the E-vector. The spectra were extracted from the red and white regions indicated in the inset STXM images, recorded at 292 eV. The spectra from the two measurements were scaled to match at the pre-edge (282 eV) and post-edge (320 eV) energies and corrected for the noncircular portion of the X-rays.[20] The spectra exhibit a sharp peak at 285.2 eV corresponding to C 1s $\rightarrow \pi^*$ transitions at sp^2 sites, and a broader peak at 291.7 eV corresponding to C 1s $\rightarrow \sigma^*$ transitions. There is no visible peak between 286 and 291 eV, indicating that the tubes were not appreciably oxidized. The π^* intensity around 285.2 eV reaches a maximum when the long axis of the nanotube is perpendicular to the E-vector of the incident polarized light ($I_\perp$), and its intensity is minimum when both nanotube and E-vector are aligned ($I_\parallel$). Such drastic behavior is explained by the angle dependence of the C 1s $\rightarrow \pi^*$ electronic excitation of the graphene-like sheets, which constitute the nanotube.[20,24] Linear dichroic intensities can be described as $I = B + A\cos^2(\theta - \theta_{ref})$, where I is the π^* resonance intensity, $(\theta - \theta_{ref})$ is the angle between the CNT long axis and the E-vector, A is the amplitude of the dichroic component, and B is a constant intensity corresponding to structural components (such as sp^2 defects) that do not exhibit dichroism. This equation has been used previously to perform quantitative analyses of the dichroic intensities of individual MWCNTs.[19]

The magnitude of the polarization dependence, which is defined as the dichroic ratio, $I_R = I_\parallel/I_\perp$, is found to differ among CNTs synthesized by different methods due to the natural density of defects associated with these methods.[19] We measure I_R for four commercially available carbon nanotubes (see Methods). It is seen that nanotubes produced by arc-discharge have lower I_R (0.10−0.15) compared to nanotubes synthesized by chemical vapor deposition (0.30−0.33). This result is associated with a smaller amount of defects present in arc-discharge nanotubes.[25,26] Indeed, for a defect-free nanotube, the π^* transition is forbidden when E is parallel to the tube and its intensity is maximum when E is perpendicular; I_R is thus close to 0.[19] The situation is very different for a tube that loses its sp^2 character at many sites through bonding to other groups or through removal of carbon atoms and subsequent buckling, deformation, and change of electronic structure. At the limit of total destruction of all sp^2 character, the material would become completely amorphous, there would be a drastic reduction in the intensity of the π^* peak, and I_R for any residual C 1s $\rightarrow \pi^*$ transition would approach 1. A nanotube containing sp^2 defects would be somewhere between those extremities, closer to one or the other, depending on the density of defects. We thus postulate that the I_R ratio can be used as a quantitative measure of the extent of non-sp^2 character (called sp^2 defects). We note that this technique, as presented here, is not sensitive to the exact type of deviations from local sp^2 character. In addition, while further investigation is needed on samples well-characterized by other techniques, such as selected area diffraction in TEM, we expect the dichroism to be most strongly related to point defects.

To demonstrate the ability of STXM to quantify defect distributions in individual carbon nanotubes, we irradiated CNTs with a 10 keV beam of Ga^+ ions using a

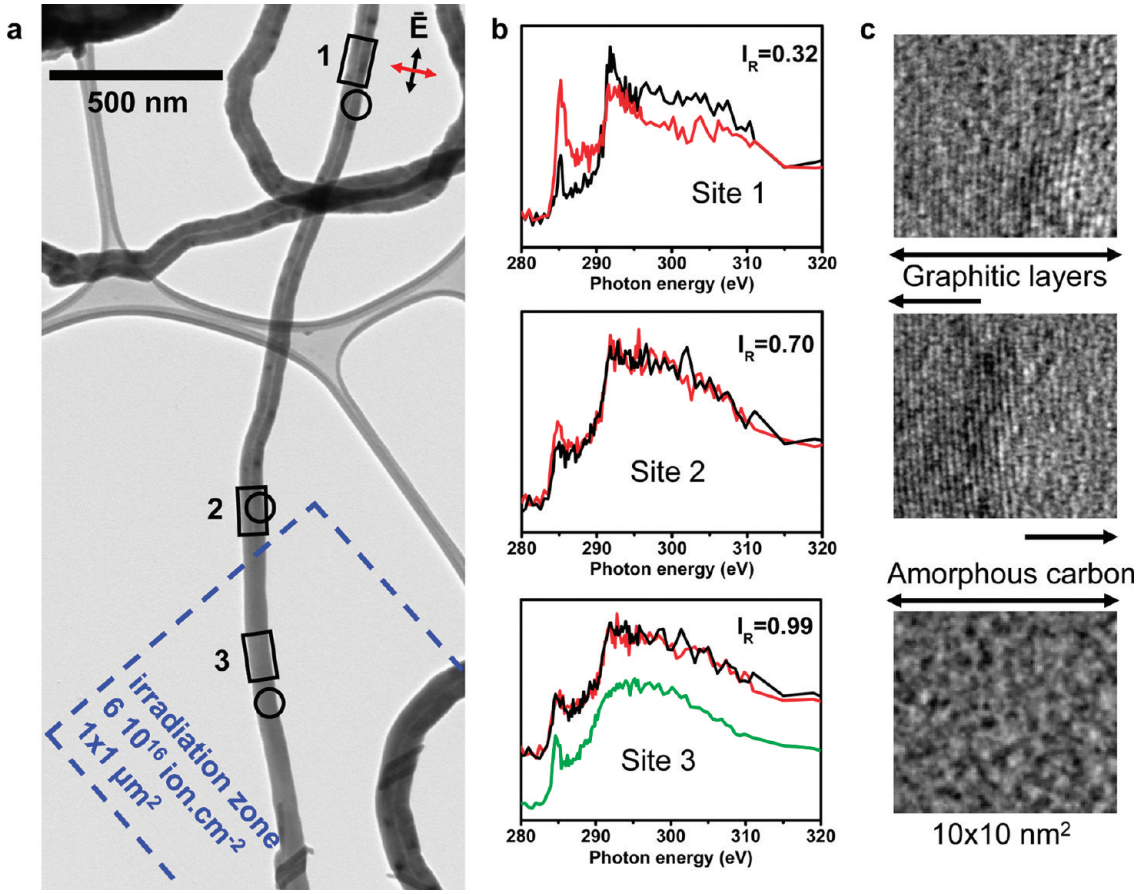

Figure 2. Characterization of defects in MWCNTs irradiated using a site-selective ion beam. (a) Transmission electron microscopy image of a MWCNT after site-selective irradiation of a 1 × 1 μm² zone (indicated in blue) with a dose of 6 × 10^{16} ions cm^{-2}. The diameter of this particular nanotube is 70 nm. STXM stacks and HRTEM images were recorded for the fully irradiated (site 3), partially irradiated (site 2), and pristine (site 1) segments as indicated by the black boxes and circles, respectively. (b) Carbon 1s NEXAFS spectra extracted from the three different sites indicated by the black boxes. The red and black curves correspond, respectively, to the nanotube oriented perpendicular and parallel to the E-vector. The ratio I_R between parallel and perpendicular π* intensities is calculated for each region. The green curve at the bottom was recorded from the amorphous carbon of the supporting TEM grid for comparison purposes. (c) High-resolution TEM images of the three regions indicated by the black circles. The images are 10 × 10 nm². (c)

focused ion beam apparatus. Figure 2a shows a TEM image of a carbon nanotube after site-selective irradiation of a 1 × 1 μm² zone with a dose of 6 × 10^{16} ions cm^{-2}. STXM stacks (a sequence of images over a range of photon energies) and HRTEM images were recorded for the fully irradiated (site 3), partially irradiated (site 2), and pristine (site 1) segments, as indicated by the black boxes and circles, respectively. For each region, C 1s stacks were recorded with both parallel and perpendicular orientation of the E-vector relative to the tubes. The corresponding NEXAFS spectra and HRTEM images of fully irradiated (site 3), partially irradiated (site 2), and pristine segments (site 1) are shown on Figure 2b,c. The red spectra correspond to the nanotube oriented perpendicular to the E-vector and the black spectra to the nanotube oriented parallel to the E-vector. The dichroic ratio calculated for each site is 0.99, 0.70, and 0.32, respectively. The I_R value for the irradiated section is very close to 1, which indicates that almost all sp^2 character is lost: this segment was transformed into an amorphous carbon nanowire by ion bombardment, as confirmed by the HRTEM analysis.

To characterize the quantitative nature of the relationship between damage and the dichroic ratio, two series of tubes with diameters of roughly 50 and 70 nm were site-selectively irradiated with various doses of ions. The polarization ratios of the irradiated areas were then measured and compared. Table 1 summarizes the results. As expected, increasing the dose results in a higher I_R, which is consistent with the expected higher

TABLE 1. Carbon 1s → π* Dichroic Ratios Measured on Two Sets of Nanotubes for Different Doses of Ion Bombardment

	$I_R = I_{\parallel}/I_{\perp}$	
dose (ions cm^{-2})	thinner CNTs (50−55 nm)	thicker CNT (70−75 nm)
6 × 10^{16}	0.99	0.99
1 × 10^{16}	1.00	0.62
1 × 10^{15}	0.71	0.50
pristine	0.30	

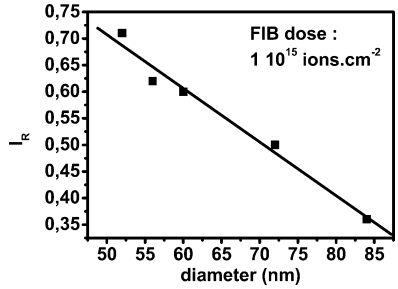

Figure 3. Nanotube diameter dependence of defect density. Dichroic ratio I_R of nanotubes irradiated with 10 keV Ga^+ ions at a dose of 10^{15} ions cm^{-2} *versus* the nanotube diameter for five MWCNTs. The line fit reveals a linear dependence.

defect density. We observe that nanotubes with different diameters exposed to the same ion dose have different I_R. The polarization ratio for the thinner MWCNTs increases from 0.30 for the pristine section to 0.71 for the area exposed to a dose of 10^{15} ions cm^{-2}; higher ion beam doses increase the polarization ratio to that of amorphous carbon (~1.00). The results shown in Table 1 suggest that complete amorphization of the thicker nanotubes occurs for ion doses higher than that for the thin nanotubes; the polarization ratio increases from 0.30 to 0.50, 0.62, and 0.99 after 10^{15}, 10^{16}, and 6×10^{16} ions cm^{-2}, respectively.

To further study the dependence of the nanotube diameter on radiation damage, we selected MWCNTs with diameters ranging from ~50 to ~85 nm and irradiated them with the same dose of 1×10^{15} ions cm^{-2}. Figure 3 plots I_R *versus* nanotube diameter for five nanotubes irradiated at 10^{15} ions cm^{-2}. The I_R decreases with increasing tube diameter. For the thin MWCNTs, I_R is close to that of amorphous carbon, indicating that they are very prone to radiation damage. In contrast, as the tubes become thicker, they become more resistant to ion irradiation. Therefore, knowing that the defect concentration is the ratio of non-sp^2 atoms to the total number of atoms in the system, it can be suggested that the depth of the ion damage is smaller than the nanotube diameter. Figure 4 displays electron microscopy images of two nanotubes of 50 and 70 nm diameter irradiated simultaneously with 10^{16} ions cm^{-2}. For the large diameter nanotube, the I_R before irradiation was 0.41. The discrepancy between this value and the value of 0.3 for pristine can be explained as follow : as can be seen from Figure 4, the larger diameter nanotube has a herringbone structure; due to the intrinsic tilted alignment of the walls, it is impossible to have the alignment between the E-vector and all walls, throughout the nanostructure. Thus, as it is expected, the non-aligned bonds contribute to the increase in the I_R value. The images in Figure 4 show that the 50 nm nanotube became completely amorphous, as indicated by an I_R value of 1. On the contrary, the larger nanotube kept its inner shells intact, consistent with a lower defect density and the measured I_R of 0.62. The resistance of the thicker tube to ion beam damage can be explained by the penetration depth of 10 keV Ga^+ ions inside a carbon nanotube. The program SRIM was used to simulate the distribution of irradiation defects in nanotubes for 10 keV Ga^+ ions.[27] The SRIM simulation predicts that, at this ion energy, damage density peaks around 10 nm

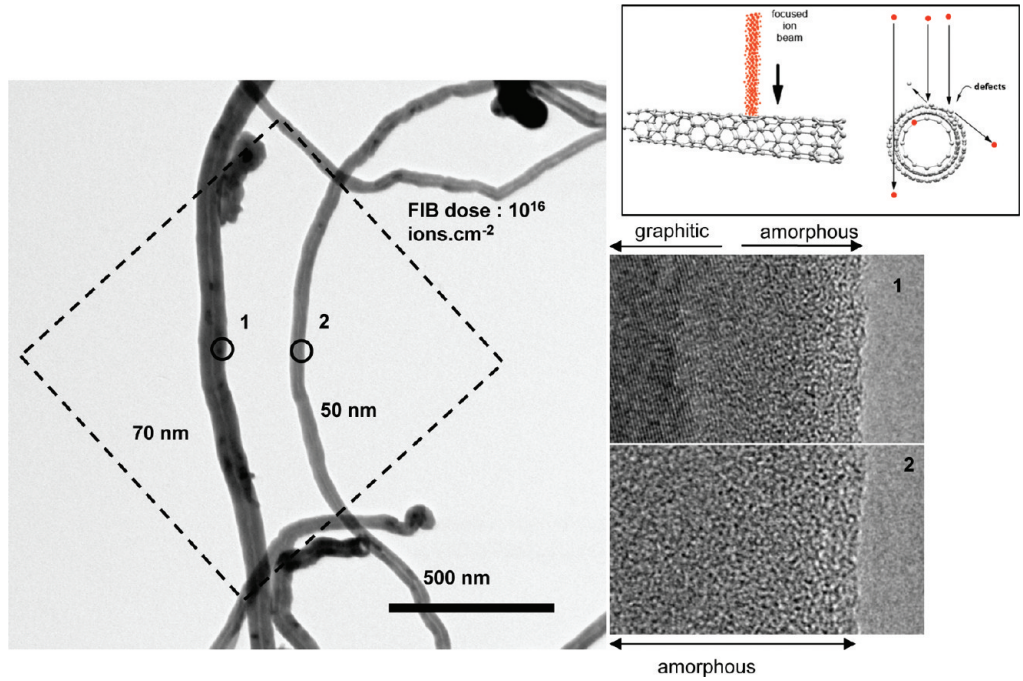

Figure 4. Penetration depth of ions in MWCNTs. Left: TEM image of two MWCNTs of 50 and 70 nm diameter irradiated with 10 keV Ga^+ ions at a dose of 10^{16} ions cm^{-2}. Right: High-resolution TEM images corresponding to regions labeled as 1 (left) and 2 (right) in the top image. The thinner nanotube is completely amorphous, while the inner graphitic structure remains intact in the large nanotube. The images are 19 × 30 nm^2.

under the surface with a profile extending to 35 nm in depth. Taking into account that SRIM is only applicable to amorphous materials and that the hollow core of a multiwalled nanotube is around 10 nm, we find that the simulation is in agreement with the defect density difference created in the 50 and 70 nm nanotubes.

In conclusion, we have demonstrated quantitative evaluation of bulk defect density in individual multiwalled carbon nanotubes based on the dichroic effect of the NEXAFS C 1s spectrum. With the support of HR-TEM, we found a clear relationship between nanotube defect density, nanotube diameter, and ion dose. In addition to probing defect density, STXM provides spectroscopy of individual CNTs, which could be useful to analyze the nature of the defects.[28] Furthermore, this technique should be suitable for studying other anisotropic nanostructures as semiconducting nanowires and oxide nanoribbons. In this study, focused ion beam irradiation is also confirmed as a powerful tool to tailor morphology and properties of individual carbon nanotubes.

METHODS

Materials. Multiwalled carbon nanotubes used in this study were purchased from SES company. These nanotubes were synthesized using a chemical vapor deposition (CVD) method. In paragraph 6, dichroic ratio is compared for two arc-discharge produced nanotubes (bought from Mercorp and n-Tec) and two CVD nanotubes (bought from SES and NanoCs). The raw powders were sonically dispersed in ethanol and a drop of the solution deposited on a lacey carbon TEM grid.

Characterization. FIB irradiation is performed using a FEI Nova 200 Nanolab Dual Beam SEM/FIB system. A standard ion column is installed which allows a Ga^+ ion beam at 5−30 keV. In this paper, nanotubes were irradiated with 10 keV Ga^+ ions at doses ranging from 10^{15} to 6×10^{16} ions cm^{-2}.

Low-resolution TEM and high-resolution TEM (HRTEM) were performed on a Tecnai 10 operated at 80 keV and FEI Tecnai G2 microscope operated at 200 keV, respectively.

To perform STXM measurements, the TEM grid is fixed on a sample holder and inserted in the experimental chamber on beamline 5.3.2 at the Advanced Light Source at the Lawrence Berkeley National Laboratory (LBNL).[29] The chamber is evacuated and then filled with 1/3 atm of helium. The monochromated X-ray beam is focused to a 30 nm spot on the sample using a Fresnel zone plate. The transmitted signal is then measured with single-photon counting using a phosphor converter and a high-performance photomultiplier tube. The energy resolution of the beamline is 150 meV, and the spatial resolution is 30 nm with the zone plates used (240 μm diameter, 25 nm outer zones, provided by the Centre for X-ray Optics, LBNL). Sample rotation was used to vary the nanotube axis with respect to the fixed E-vector.[30]

While spectra can be measured in point or line modes, the most useful mode for studies of nano-objects such as CNTs is the image sequence or stack mode, in which images are measured at each photon energy in a sequence. This is functionally equivalent to recording a full absorption spectrum at each pixel and is analogous to energy-filtered TEM (EF-TEM) mode in TEM-EELS. In this work, C 1s stacks were recorded with pixel size of 20 nm and a dwell time of 1 ms.

Some of the measurements were performed on beamline 10ID1 at the Canadian Light Source.[31] In this case, the dichroic signal is recorded by using an EPU to rotate the E-vector in the plane of the fixed sample. Spectral intensities from STXM532 were corrected for the incomplete polarization of the incident light. At the ALS bend magnet beamline, the X-rays were measured to be 82 ± 5% linearly polarized.[32] At the CLS, the X-rays are generated by an Apple-II type EPU, which produces essentially 100% linearly polarized light for which the spatial orientation of the E-vector can be adjusted over the range of +90° to −90° by changing the relative positions of the quadrants (phase) of the EPU.

SRIM Simulations. SRIM calculations were performed for Ga ions implanted in a carbon target of 1.7 g/cm^3 with a displacement energy of 15 eV.[33] SRIM code allows simulating the damage depth profile at different Ga^+ ion energy. At 10 keV, Ga^+ ions damage the nanotube on the uppermost 35 nm with a damage density peaking at 10 nm. It is also worth mentioning that the Ga^+ ions are implanted in the nanotube. This effect can be lowered by using higher energy and smaller nanotubes.

Acknowledgment. This work was supported by the Nanobeams EU Network of Excellence and the EU-STREP Project Nano2hybrids (No. 033311) and the NSERC, CFI, and Canada Research Chair. STXM measurements were carried out at beamline 5.3.2 at the Advanced Light Source (ALS), which is supported by the Office of Basic Energy Sciences of the U.S. Department of Energy under Contract DE-AC03-76SF00098. The Canadian Light Source (CLS) is supported by the Canada Foundation for Innovation (CFI), NSERC, CIHR, NRC, and the University of Saskatchewan. We thank Tolek Tyliszczak and David Kilcoyne for their expert support of the ALS STXMs, and Konstantine Kaznatcheev, Chithra Karunakaran, and Jian Wang for their support of the CLS STXM. The support of the COST Action MP0901 "NanoTP" is gratefully acknowledged.

REFERENCES AND NOTES

1. Krasheninnikov, A. V.; Banhart, F. Engineering of Nanostructured Carbon Materials with Electron or Ion Beams. *Nat. Mater.* **2007**, *6*, 723–733.
2. Buongiorno Nardelli, M.; Fattebert, J.-L.; Orlikowski, D.; Roland, C.; Zhao, Q.; Bernholc, J. Mechanical Properties, Defects and Electronic Behavior of Carbon Nanotubes. *Carbon* **2000**, *38*, 1703–1711.
3. Charlier, J. C. Defects in Carbon Nanotubes. *Acc. Chem. Res.* **2002**, *35*, 1063–1069.
4. Raghuveer, M. S.; Kumar, A.; Frederick, M. J.; Louie, G. P.; Ganesan, P. G.; Ramanath, G. Site-Selective Functionalization of Carbon Nanotubes. *Adv. Mater.* **2006**, *18*, 547–552.
5. Gómez-Navarro, C.; De Pablo, P. J.; Gomez-Herrero, J.; Biel, B.; Garcia-Vidal, F. J.; Rubio, A.; Flores, F. Tuning the Conductance of Single Walled Carbon Nanotubes by Ion Irradiation in the Anderson Localization Regime. *Nat. Mater.* **2005**, *4*, 534–539.
6. Felten, A.; Bittencourt, C.; Colomer, J.-F.; Van Tendeloo, G.; Pireaux, J.-J. Nucleation of Metal Clusters on Plasma Treated Multi Wall Carbon Nanotubes. *Carbon* **2007**, *45*, 110–116.
7. Horvath, Z. E.; Koos, A. A.; Kertesz, K.; Molnar, G.; Vertesy, G.; Bein, M. C.; Frigyes, T.; Meszaros, Z.; Gyulai, J.; Biro, L. P. The Role of Defects in Chemical Sensing Properties of Carbon Nanotube Films. *Appl. Phys. A: Mater. Sci. Process.* **2008**, *93*, 495–504.
8. Jung, Y. J.; Homma, Y.; Vajtai, R.; Kobayashi, Y.; Ogino, T.; Ajayan, P. M. Straightening Suspended Single Walled Carbon Nanotubes by Ion Irradiation. *Nano Lett.* **2004**, *4*, 1109–1113.
9. Terrones, M.; Banhart, F.; Grobert, N.; Charlier, J. C.; Terrones, H.; Ajayan, P. M. Molecular Junctions by Joining Single-Walled Carbon Nanotubes. *Phys. Rev. Lett.* **2002**, *89*, 075505.
10. Gopal, V.; Radmilovic, V. R.; Daraio, C.; Jin, S.; Yang, P. D.;

Stach, E. A. Rapid Prototyping of Site-Specific Nanocontacts by Electron and Ion Beam Assisted Direct-Write Nanolithography. *Nano Lett.* **2004**, *4*, 2059–2063.
11. Khan, F. M. *The Physics of Radiation Therapy*, 4th ed.; Lippincott Williams & Wilkins: Baltimore, MD, 2009.
12. Leffers, T.; Singh, B. *Jernkontorets Ann.* **1981**, *165*, 58–62.
13. Banhart, F. Irradiation Effects in Carbon Nanostructures. *Rep. Prog. Phys.* **1999**, *62*, 1181–1221.
14. Doorn, S. K.; Zheng, L. X.; O'Connell, M. J.; Zhu, Y. T.; Huang, S. M.; Liu, J. Raman Spectroscopy and Imaging of Ultralong Carbon Nanotubes. *J. Phys. Chem. B* **2005**, *109*, 3751–3758.
15. Fan, Y.; Goldsmith, B. R.; Collins, P. G. Indentifying and Counting Point Defects in Carbon Nanotubes. *Nat. Mater.* **2005**, *4*, 906–911.
16. Sfeir, M. Y.; Wang, F.; Huang, L. M.; Chuang, C. C.; Hone, J.; O'Brien, S. P.; Heinz, T. F.; Brus, L. E. Probing Electronic Transitions in Individual Carbon Nanotubes by Rayleigh Scattering. *Science* **2004**, *306*, 1540–1543.
17. Chakraborty, A. K.; Woolley, R. A. J.; Butenko, Y. V.; Dhanak, V. R.; Siller, L.; Hunt, M. R.C. A Photoelectron Spectroscopy Study of Ion-Irradiation Induced Defects in Single-Wall Carbon Nanotubes. *Carbon* **2007**, *45*, 2744–2750.
18. Chao, W.; Harteneck, B. D.; Liddle, J. A.; Anderson, E. H.; Attwood, D. T. Soft X-ray Microscopy at Spatial Resolution Better than 15 nm. *Nature* **2005**, *435*, 1210–1213.
19. Najafi, E.; Hernández-Cruz, D.; Obst, M.; Hitchcock, A. P.; Douhard, B.; Pireaux, J. J.; Felten, A. Polarization Dependence of the C 1s X-ray Absorption Spectra of Individual Multi-Walled Carbon Nanotubes. *Small* **2008**, *4*, 2279–2285.
20. Najafi, E.; Hernández-Cruz, D.; Obst, M.; Hitchcock, A. P.; Felten, A.; Douhard, B.; Pireaux, J. J.; Kaznatcheev, K.; Karunakaran, C. Scanning Transmission X-ray Microscopy of Multi-Walled Carbon Nanotubes. *J. Phys. Conf. Ser.* **2009**, *186*, 012106-9.
21. Egerton, R. F. *Electron Energy-Loss Spectroscopy in the Electron Microscope*, 2nd ed.; Plenum Press: New York, 1996.
22. Bosman, M.; Watanabe, M.; Alexander, D. T. L.; Keast, V. J. Mapping Chemical and Bonding Information Using Multivariate Analysis of Electron Energy-Loss Spectrum Images. *Ultramicroscopy* **2006**, *106*, 1024–1032.
23. Bosman, M.; Keast, V. J.; Watanabe, M.; McCulloch, D. G.; Shakerzadeh, M.; Teo, E. H. T.; Tay, B. K. Quantitative, Nanoscale Mapping of sp^2 Percentage and Crystal Orientation in Carbon Multilayers. *Carbon* **2009**, *47*, 94–101.
24. Banerjee, S.; Hemraj-Benny, T.; Sambasivan, S.; Fischer, D. A.; Misewich, J. A.; Wong, S. S. Near-Edge X-ray Absorption Fine Structure Investigations of Order in Carbon Nanotube-Based Systems. *J. Phys. Chem. B* **2005**, *109*, 8489–8495.
25. Grobert, N. Carbon Nanotubes—Becoming Clean. *Mater. Today* **2007**, *10*, 28–35.
26. Felten, A.; Bittencourt, C.; Pireaux, J. J.; Reichelt, M.; Mayer, J.; Hernandez-Cruz, D.; Hitchcock, A. P. Individual Multiwall Carbon Nanotube Spectroscopy by Scanning Transmission X-ray Microscopy. *Nano Lett.* **2007**, *7*, 2435–2440.
27. Biersack, J. P.; Haggmark, L. A Monte Carlo Computer Program for the Transport of Energetic Ions in Amorphous Targets. *Nucl. Instrum. Methods* **1980**, *174*, 257–269. http://www.srim.org.
28. Gao, B.; Wu, Z. Y.; Agren, H.; Luo, Y. Chirality and Diameter Dependent X-ray Absorption of Single Walled Carbon Nanotubes. *J. Chem. Phys.* **2009**, *131*, 034704-10.
29. Kilcoyne, A. L. D.; Tyliszczak, T.; Steele, W. F.; Fakra, S.; Hitchcock, P.; Franck, K.; Anderson, E.; Harteneck, B.; Rightor, E. G.; Mitchell, G. E.; Hitchcock, A. P.; Yang, L.; Warwick, T.; Ade, H. Interferometer-Controlled Scanning Transmission X-ray Microscopes at the Advanced Light Source. *J. Synchrotron Radiat.* **2003**, *10*, 125–136.
30. Hernández-Cruz, D.; Hitchcock, A. P.; Tyliszczak, T.; Rousseau, M.-E.; Pézolet, M. *In Situ* Azimuthal Rotation Device for Linear Dichroism Measurements in Scanning Transmission X-ray Microscopy. *Rev. Sci. Instrum.* **2007**, *78*, 033703-9.
31. Kaznatcheev, K. V.; Karunakaran, Ch.; Lanke, U. D.; Urquhart, S. G.; Obst, M.; Hitchcock, A. P. Soft X-ray Spectromicroscopy Beamline at the CLS: Commissioning Results. *Nucl. Instrum. Methods Phys. Res., Sect. A* **2007**, *582*, 96–99.
32. Watts, B.; Ade, H. A Simple Method for Determining Linear Polarization and Energy Calibration of Focused Soft X-ray Beams. *J. Electron Spectrosc. Relat. Phenom.* **2008**, *162*, 49–55.
33. Kim, S. H.; Mulholland, G. W.; Zachariah, M. R. Density Measurement of Size Selected Multiwalled Carbon Nanotubes by Mobility-Mass Characterization. *Carbon* **2009**, *47*, 1297–1302.